FAR FIELD SPLITTING FOR THE HELMHOLTZ EQUATION

ROLAND GRIESMAIER*, MARTIN HANKE†, AND JOHN SYLVESTER‡

Abstract. Given far field data of a time-harmonic wave radiated by an ensemble of well separated acoustic or electromagnetic sources as well as a priori information on the locations of these sources, we discuss an algorithm to approximate the far field data radiated by each of these sources separately. The method is based on a Galerkin procedure considering subspaces spanned by the singular vectors of "restricted" far field operators that map local source distributions to the corresponding radiated far field patterns. We provide an error analysis for this algorithm and consider its stability. Furthermore, we exemplify a means to extract the required a priori knowledge directly from the far field data, and we show how to utilize the split far fields to recover information on the supports of the individual sources beyond that a priori information. Numerical results for the most important example of inverse obstacle scattering illustrate our theoretical findings.

Version from May 24, 2013.

Key words. Inverse source problem, inverse scattering, Helmholtz equation, source splitting, convex scattering support, inverse Radon approximation

AMS subject classifications. 35R30, 65N21

1. Introduction. We continue our previous investigations of the inverse source problem for the two-dimensional Helmholtz equation as a means to provide inversion methods for inverse scattering from a medium or an obstacle for one fixed excitation only, given the far field pattern of the corresponding scattered field. As one outcome of these works the third author, together with Kusiak [8, 9], developed the concept of the convex scattering support, which is the smallest convex set that supports a source that is compatible with the given far field data. Although this set provides relevant information regardless of whether the scatterer is one single obstacle or an ensemble of separate objects, it does not allow (as it stands) to distinguish between different scatterers, as the "reconstruction" is one convex set, and nothing more; not even the number of the present obstacles can be guessed from the convex scattering support.

In [12] the notion of convex scattering support has been extended, introducing the so-called UWSC-support: This concept associates to any far field pattern the smallest union of well separated convex (UWSC) sets that supports a source that can radiate it. While stable methods for reconstructing the convex scattering support from the far field data are available (see [9, 11]), no such algorithm has been proposed for the UWSC-support so far.

In [5] the second author suggested a means to locate vertices or other individual boundary points of the obstacles by determining certain rational approximations of the scattered field; while this approach seems capable of separating different scatterers, its practical application is limited because the method is extremely unstable (as it stands) and thus requires very accurate measurements.

The same data can be inverted using yet another imaging scheme developed in [4]; this method builds upon a windowed Fourier transform of the far field data, followed

---

*Mathematisches Institut, Universität Leipzig, 04009 Leipzig, Germany (`griesmaier@math.uni-leipzig.de`)

†Institut für Mathematik, Johannes Gutenberg-Universität Mainz, 55099 Mainz, Germany (`hanke@math.uni-mainz.de`)

‡Department of Mathematics, University of Washington, Seattle, Washington 98195, U.S.A. (`sylvest@u.washington.edu`). This research was supported in part by NSF grant DMS-1007447

by a filtered backprojection. We shall call this the inverse Radon approximation. The reconstruction does provide information about the number of scatterers and their locations, but the reconstructed images are extremely blurry when the wave number is close to the resonance region of an individual obstacle.

In this work we propose an algorithm that builds upon some of the aforementioned techniques and combines them to benefit from their individual advantages. The method consists of three steps: The first step utilizes the reconstruction obtained from the inverse Radon approximation to estimate the number and the centers of the well-separated scatterers that are present. In step two we use this information to split the given far field into a sum of components, each of which approximates the far field of an individual scatterer. In the final step we then determine the convex scattering support of each individual far field component separately, to provide more accurate information about the shape of the scatterers than is contained in the inverse Radon approximation.

The novel mathematical contribution in this work is a constructive means and associated analysis of how to perform the splitting step. The idea of splitting the far field of an ensemble of scatterers into individual pieces has already been proposed in earlier work by Ben Hassen, Liu, and Potthast [6] (see also [10]); however, their approach is based on the solution of severely ill-posed integral equations and, so far, lacks a rigorous stability analysis. Our method comes with a decent stability analysis and is rather straightforward to implement.

The outline of our paper is as follows: In Section 2 we provide the necessary theoretical background of the forward model (the source problem for the two-dimensional Helmholtz equation with a compactly supported source) and the Fourier analysis of the resulting far field. Assuming that two well separated disks in space are known that contain all individual components of the source we go on in Section 3 and propose a Galerkin ansatz – in accordance with the aforementioned Fourier analysis – to split the far field in two individual components corresponding to the union of sources in each of the two balls, respectively. In Section 4 we discuss the stability of this procedure, and we provide safeguards to discard mistaken approximations. In Section 5 we extend this approach to more than two source components. Sections 6 and 7 provide two examples that illustrate how the combination of the inverse Radon approximation and the convex scattering support technique can provide approximations of multiple individual scatterers from the far field pattern of the field scattered by a single excitation.

2. The Fourier expansion of a far field pattern. Given a compactly supported function

$$f \in L_0^2(\mathbb{R}^2) := \{f \in L^2(\mathbb{R}^2) \mid \operatorname{supp} f \subset \mathbb{R}^2 \text{ compact}\}$$

and a fixed *wave number* $\kappa > 0$ we consider the *source problem* for the Helmholtz equation

$$-\Delta u - \kappa^2 u = f \qquad \text{in } \mathbb{R}^2 . \tag{2.1a}$$

The physically relevant solution u of (2.1a) satisfies the *Sommerfeld radiation condition*

$$\lim_{r \to \infty} \sqrt{r} \left(\frac{\partial u}{\partial r} - \mathrm{i}\kappa u \right) = 0 \qquad \text{for } |x| = r , \tag{2.1b}$$

and can be written as a volume potential

$$u(x) = \int_{\mathbb{R}^2} \Phi_\kappa(x - y) f(y) \, \mathrm{d}y, \qquad x \in \mathbb{R}^2,$$

where

$$\Phi_\kappa(x) := \frac{\mathrm{i}}{4} H_0^{(1)}(\kappa|x|), \qquad x \neq 0,$$

denotes the *fundamental solution* of the two-dimensional Helmholtz equation. It is well known (see, e.g., Colton and Kress [1]) that u has the asymptotic behavior

$$u(x) = \frac{e^{\mathrm{i}\pi/4}}{\sqrt{8\pi\kappa}} \frac{e^{\mathrm{i}\kappa|x|}}{\sqrt{|x|}} u^\infty(\widehat{x}) + O\left(|x|^{-3/2}\right) \qquad \text{as } |x| \to \infty,$$

where $\widehat{x} := x/|x|$ and

$$u^\infty(\widehat{x}) = \int_{\mathbb{R}^2} e^{-\mathrm{i}\kappa\widehat{x}\cdot y} f(y) \, \mathrm{d}y = \widehat{f}(\kappa\widehat{x}), \qquad \widehat{x} \in S^1, \tag{2.2}$$

is the so-called *far field pattern* of u. Here, $\widehat{f}$ denotes the Fourier transform of f. We refer to f as the *source* and to u^∞ as the *far field radiated by* f. Accordingly, the operator $\mathcal{F} : L_0^2(\mathbb{R}^2) \to L^2(S^1)$,

$$\mathcal{F}f := \widehat{f}|_{\kappa S^1},$$

which maps the source f to its far field pattern, is called the *far field operator*.

Using polar coordinates $\widehat{x} = (\cos t, \sin t)$ and $y = |y|(\cos\varphi_y, \sin\varphi_y)$ with $t, \varphi_y \in [0, 2\pi)$, the Jacobi-Anger expansion (see, e.g., [1]) reads

$$e^{\pm\mathrm{i}\kappa\widehat{x}\cdot y} = \sum_{n=-\infty}^{\infty} (\pm\mathrm{i})^n e^{-\mathrm{i}n\varphi_y} J_n(\kappa|y|) e^{\mathrm{i}nt}. \tag{2.3}$$

Therefore, the far field pattern u^∞ radiated by f satisfies

$$u^\infty(\widehat{x}) = \sum_{n=-\infty}^{\infty} a_n e^{\mathrm{i}nt}, \qquad \widehat{x} \in S^1, \tag{2.4}$$

with Fourier coefficients

$$a_n = (-\mathrm{i})^n \int_{\mathbb{R}^2} e^{-\mathrm{i}n\varphi_y} J_n(\kappa|y|) f(y) \, \mathrm{d}y. \tag{2.5}$$

Assuming that the source f is supported in the disk $B_r(0)$ of radius $r > 0$ around the origin, the Fourier coefficients of the corresponding radiated far field are essentially supported in the index range $|n| \lesssim \kappa r$, and decay superlinearly as function of $|n|$, cf., e.g., Gradshteyn and Ryzhik [3, 8.402],

$$|J_n(\kappa r)| \approx \frac{1}{\sqrt{2\pi|n|}} \left(\frac{\kappa e r}{2|n|}\right)^{|n|} \left(1 + O\left(\frac{1}{|n|}\right)\right) \qquad \text{for } |n| \to \infty.$$

More precisely, there holds

$$|J_n(\kappa r)| \leq \begin{cases} 1, & |n| \leq e\kappa r/2, \\ \left(\dfrac{\kappa e r}{2|n|}\right)^{|n|}, & |n| \geq e\kappa r/2, \end{cases} \tag{2.6}$$

cf. Theorem A.1 in the Appendix.

For fixed $N > 0$ and u^∞ as in (2.4) we introduce the operator $Q_N : L^2(S^1) \to L^2(S^1)$ given by

$$Q_N u^\infty := \sum_{n=-N}^{N} a_n e^{\mathrm{i} n t}, \tag{2.7}$$

which is just the orthogonal projection of u^∞ onto its $2N + 1$ lowest order Fourier modes.

Next we construct a source supported in $B_r(0)$ that radiates the far field $Q_N u^\infty$ defined in (2.7). To this end we introduce for a given bounded domain $\Omega \subset \mathbb{R}^2$ the *restricted far field operator* $\mathcal{F}_\Omega : L^2(\Omega) \to L^2(S^1)$ given by

$$\mathcal{F}_\Omega f := \widehat{f}|_{\kappa S^1},$$

where $\widehat{f}$ is the Fourier transform of $\tilde{f}$, the extension of f which is identically zero in $\mathbb{R}^2 \setminus \Omega$. $\mathcal{F}_\Omega$ is a compact integral operator, cf. (2.2), whose adjoint is the Herglotz operator $\mathcal{F}_\Omega^* : L^2(S^1) \to L^2(\Omega)$,

$$(\mathcal{F}_\Omega^* g)(y) = \int_{S^1} e^{\mathrm{i}\kappa\widehat{x}\cdot y} g(\widehat{x}) \, \mathrm{d}s(\widehat{x}), \qquad y \in \Omega.$$

Using the one-to-one correspondence between Herglotz wave functions and their kernels (cf. [1, Theorem 3.15]) it follows immediately that $\mathcal{F}_\Omega^*$ is injective, and thus $\mathcal{F}_\Omega$ has dense range. For $\Omega = B_r(0)$ we have explicit knowledge of the singular system $(\frac{s_n(\kappa r)}{\kappa}; u_n, v_n)$, $n \in \mathbb{Z}$ of $\mathcal{F}_{B_r(0)}$, cf., e.g., [9, p. 1147]: It is given by $u_n(\widehat{x}) = (1/\sqrt{2\pi}) \, e^{\mathrm{i} n t}$, $\widehat{x} = (\cos t, \sin t) \in S^1$,

$$s_n^2(\kappa r) = 2\pi\kappa^2 \int_{B_r(0)} J_n^2(\kappa|x|) \, \mathrm{d}x,$$

and

$$v_n(x) = \frac{\kappa\sqrt{2\pi}}{s_n(\kappa r)} \mathrm{i}^n J_n(\kappa|x|) e^{\mathrm{i} n\varphi_x}, \qquad x = |x|(\cos\varphi_x, \sin\varphi_x) \in B_r(0).$$

Therewith, we find that the right-hand side of (2.7) is the far field of the source

$$f(x) = \begin{cases} 2\pi\kappa^2 \displaystyle\sum_{n=-N}^{N} \dfrac{a_n}{s_n^2(\kappa r)} \mathrm{i}^n e^{\mathrm{i} n\varphi_x} J_n(\kappa|x|), & |x| < r, \\ 0 & |x| \geq r, \end{cases} \tag{2.8}$$

supported in $B_r(0)$.

REMARK 2.1. Note that, using the same procedure as in (2.8), we can construct – for all $\varepsilon > 0$ – sources f_ε that radiate the same far field $Q_N u^\infty$ from (2.7) and are

supported in the balls $B_\varepsilon(0)$ of radius ε around the origin. As ε decreases, however, the L^2 norms of the f_ε will increase because the $s_n^2(\kappa r)$ increase monotonically with r. It is worth remarking that the sources constructed in (2.8) minimize the L^2 norm among all sources, supported in $B_r(0)$, that radiate the far field $Q_N u^\infty$.

We say that a compact set $\Omega \subset \mathbb{R}^2$ *carries* a given far field u^∞, if every open neighborhood of Ω supports a source that radiates that far field. The *convex scattering support* $\mathscr{C}(u^\infty)$ of u^∞ is defined as the intersection of all compact convex sets that carry that far field. In particular, the convex scattering support of $Q_N u^\infty$ is the set containing the origin only, i.e., it consists of a single point.   ◇

In the following lemma we establish an approximation error estimate for the projection Q_N from (2.7).

LEMMA 2.2. *Let $f \in L_0^2(\mathbb{R}^2)$ with* $\operatorname{supp} f \subset B_r(0)$*, and denote by $u^\infty \in L^2(S^1)$ the corresponding radiated far field pattern. Then, assuming $N \geq \kappa r/2$, there holds*

$$\|u^\infty - Q_N u^\infty\|_{L^2(S^1)} \leq \frac{r\sqrt{2\pi}}{\sqrt{N+1}} \left(\frac{\kappa e r}{2N}\right)^N \|f\|_{L^2(\mathbb{R}^2)}. \tag{2.9}$$

Proof. To begin with, we use (2.6) to deduce that

$$\begin{aligned} s_n^2(\kappa r) &= (2\pi)^2 \kappa^2 \int_0^r J_n^2(\kappa\rho)\rho \, \mathrm{d}\rho \\ &\leq (2\pi)^2 \kappa^2 \int_0^r \left(\frac{\kappa e \rho}{2n}\right)^{2n} \rho \, \mathrm{d}\rho = \frac{2\pi^2(\kappa r)^2}{n+1}\left(\frac{\kappa e r}{2n}\right)^{2n}. \end{aligned} \tag{2.10}$$

The superlinearly decaying factor on the right-hand side of (2.10) is a decreasing function of n, for n bigger than $\kappa r/2$. In terms of the singular system of the restricted far field operator $\mathcal{F}_{B_r(0)}$, we now can write $f = \sum_{n=-\infty}^{\infty} f_n v_n$, where

$$f_n = \int_{B_r(0)} \frac{\kappa\sqrt{2\pi}}{s_n(\kappa r)}(-\mathrm{i})^n J_n(\kappa|x|)e^{-in\varphi_x} f(x) \, \mathrm{d}x = \frac{\kappa\sqrt{2\pi}\, a_n}{s_n(\kappa r)},$$

cf. (2.5). Therefore, when $N \geq \kappa r/2$, there holds

$$\|u^\infty - Q_N u^\infty\|_{L^2(S^1)}^2 = \left\|\sum_{|n|>N} a_n e^{int}\right\|_{L^2(S^1)}^2 = \left\|\sum_{|n|>N} \frac{s_n(\kappa r)}{\kappa} f_n u_n\right\|_{L^2(S^1)}^2$$

$$\leq \frac{r^2 2\pi^2}{N+1}\left(\frac{\kappa e r}{2N}\right)^{2N} \|f\|_{L^2(\mathbb{R}^2)}^2,$$

i.e., (2.9).   □

If the source f is not supported in $B_r(0)$ but in $B_r(z)$ with $z \neq 0$ we can shift it into $B_r(0)$ by means of the translation operator $f \mapsto \widetilde{f} = f(\,\cdot\, + z)$. Recalling how the Fourier transform interacts with translations, we find that the far field pattern $\widetilde{u}^\infty$ radiated by $\widetilde{f}$ satisfies

$$\widetilde{u}^\infty(\widehat{x}) = (M_z u^\infty)(\widehat{x}), \qquad \widehat{x} \in S^1, \tag{2.11}$$

where as before u^∞ denotes the far field radiated by f and $M_z : L^2(S^1) \to L^2(S^1)$ is the multiplication operator given by

$$(M_z \phi)(\widehat{x}) = e^{i\kappa\widehat{x}\cdot z}\phi(\widehat{x}), \qquad \widehat{x} \in S^1. \tag{2.12}$$
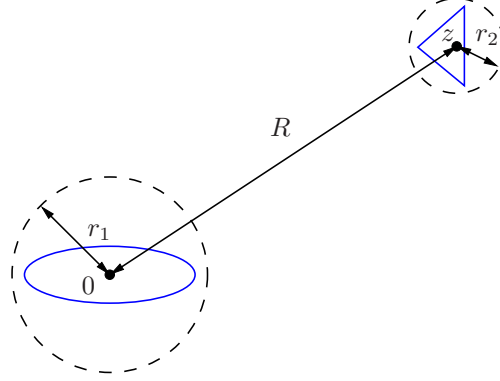
FIG. 3.1. *Sketch of the geometry.*

Note that M_z is a unitary operator, i.e., $M_z^{-1} = M_z^*$. Combining (2.11) and (2.3) the Fourier coefficients of

$$\widetilde{u}^\infty(\widehat{x}) = \sum_{m=-\infty}^{\infty} \widetilde{a}_m e^{imt}, \qquad \widehat{x} \in S^1,$$

are then obtained by a convolution of the Fourier coefficients of $e^{i\kappa\widehat{x}\cdot z}$, cf. (2.3), with those of u^∞, i.e., writing $z = R(\cos\varphi_z, \sin\varphi_z)$,

$$\widetilde{a}_m = \sum_{n=-\infty}^{\infty} i^{n-m} e^{i(n-m)\varphi_z} J_{n-m}(\kappa R) a_n, \qquad m \in \mathbb{Z}. \tag{2.13}$$

3. Splitting far field patterns that are radiated from two well separated domains. Next we assume that the far field u^∞ in (2.2) is a superposition

$$u^\infty = u_1^\infty + u_2^\infty \tag{3.1}$$

of two far fields u_1^∞ and u_2^∞ that are radiated from $B_{r_1}(0)$ and $B_{r_2}(z)$, respectively, where $|z| = R > r_1 + r_2$. By this we mean that there exist sources $f_j \in L_0^2(\mathbb{R}^2)$, $j = 1, 2$, such that $\operatorname{supp} f_1 \subset B_{r_1}(0)$, $\operatorname{supp} f_2 \subset B_{r_2}(z)$, and $\mathcal{F}f_j = u_j^\infty$ (see Fig. 3.1 for a sketch of the geometrical setup).

The decomposition on the right hand side of (3.1) is uniquely determined. In fact, given any two bounded domains $\Omega_1, \Omega_2 \subset \mathbb{R}^2$ such that $\mathbb{R}^2 \setminus \Omega_1$ and $\mathbb{R}^2 \setminus \Omega_2$ are connected and $\overline{\Omega_1} \cap \overline{\Omega_2} = \emptyset$, and denoting by $\mathcal{F}_{\Omega_j}$, $j = 1, 2$, the corresponding restricted far field operators, it follows immediately from [12, Lemma 6] that

$$\mathcal{R}(\mathcal{F}_{\Omega_1}) \cap \mathcal{R}(\mathcal{F}_{\Omega_2}) = \{0\}. \tag{3.2}$$

In order to compute approximations of u_j^∞, $j = 1, 2$, from u^∞ and the knowledge of r_1, r_2 and z, we denote by Q_{N_j}, $j = 1, 2$, the orthogonal projections from (2.7) corresponding to truncation indices N_j instead of N. Defining

$$P_1 := Q_{N_1} \qquad \text{and} \qquad P_2 := M_z^* Q_{N_2} M_z, \tag{3.3}$$

we observe that $P_2^2 = P_2$ and $P_2^* = P_2$, and therefore P_2 is an orthogonal projection as well: It projects a function from $L^2(S^1)$ onto the far fields radiated by sources of

the form (2.8), after having been shifted from the neighborhood of the origin into the corresponding neighborhood of z.

LEMMA 3.1. *If $z \neq 0$ then there holds $\|P_1 P_2\| = \|P_2 P_1\| < 1$.*

Proof. As P_1 and P_2 are orthogonal projections, $P_2 P_1 = (P_1 P_2)^*$, and hence, $P_1 P_2$ and $P_2 P_1$ have the same norm. As $\mathcal{R}(P_1)$ and $\mathcal{R}(P_2)$ are subspaces of $\mathcal{R}(\mathcal{F}_{\Omega_1})$ and $\mathcal{R}(\mathcal{F}_{\Omega_2})$, respectively, they also have trivial intersection. They are finite dimensional, hence closed, whence it follows (see, e.g., Deutsch [2]) that $\|P_1 P_2\| < 1$. $\qquad\square$

In the following we seek approximations $v_j^\infty \in \mathcal{R}(P_j)$ of u_j^∞, $j = 1, 2$, satisfying the Galerkin condition

$$\langle v_1^\infty + v_2^\infty, \phi \rangle_{L^2(S^1)} = \langle u^\infty, \phi \rangle_{L^2(S^1)} \qquad \text{for all } \phi \in \mathcal{R}(P_1) \oplus \mathcal{R}(P_2) . \qquad (3.4)$$

Choosing $\phi = P_j \psi$, $j = 1, 2$, for some $\psi \in L^2(S^1)$ in (3.4) yields

$$\langle P_j v_1^\infty, \psi \rangle_{L^2(S^1)} + \langle P_j v_2^\infty, \psi \rangle_{L^2(S^1)} = \langle P_j u^\infty, \psi \rangle_{L^2(S^1)} \qquad \text{for all } \psi \in L^2(S^1) ,$$

which implies that

$$v_1^\infty + P_1 v_2^\infty = P_1 u^\infty , \qquad (3.5a)$$
$$P_2 v_1^\infty + v_2^\infty = P_2 u^\infty . \qquad (3.5b)$$

Obviously, (3.4) and (3.5) are equivalent. Viewing the latter as a two-by-two block system and recalling Lemma 3.1, a Neumann series argument shows that both problems have a unique solution $(v_1, v_2) \in \mathcal{R}(P_1) \times \mathcal{R}(P_2)$.

Applying P_1 to both sides of (3.5b) and substituting the result into (3.5a), the system (3.5) decouples and we obtain that

$$(I - P_1 P_2 P_1) v_1^\infty = P_1 (I - P_2) u^\infty , \qquad (3.6a)$$

where we have used the projection property $P_1 u_1^\infty = u_1^\infty$. Similarly,

$$(I - P_2 P_1 P_2) v_2^\infty = P_2 (I - P_1) u^\infty . \qquad (3.6b)$$

Note that, once again using a Neumann series argument, both equations (3.6a) and (3.6b) have a unique solution $v_j \in \mathcal{R}(P_j)$, $j = 1, 2$, as well. Since solutions to (3.5) clearly solve (3.6), these systems are equivalent. We mention that the two equations (3.6) are the Schur complement systems associated with the block system (3.5), and hence, are better conditioned to solve numerically.

The following lemma contains an error estimate for this Galerkin approximation.

LEMMA 3.2. *Suppose $u^\infty = u_1^\infty + u_2^\infty$ is the superposition of two far field patterns radiated from sources f_1 and f_2 supported in $B_{r_1}(0)$ and $B_{r_2}(z)$, respectively, where $|z| = R > r_1 + r_2$. Choosing truncation indices $N_j = \lceil \alpha \kappa r_j \rceil$, $j = 1, 2$, with $\alpha \geq e/2$, we denote by $v_1^\infty \in \mathcal{R}(P_1)$ and $v_2^\infty \in \mathcal{R}(P_2)$ the corresponding Galerkin approximations solving (3.4). Then,*

$$\|u^\infty - (v_1^\infty + v_2^\infty)\|_{L^2(S^1)} \leq \left(\max_{j=1,2} q_j \right) \left(\|f_1\|_{L^2(B_{r_1}(0))} + \|f_2\|_{L^2(B_{r_2}(z))} \right) , \qquad (3.7)$$

where $q_j = \frac{r_j \sqrt{2\pi}}{\sqrt{N_j + 1}} (e/(2\alpha))^{\alpha \kappa r_j}$, $j = 1, 2$.

Proof. From (3.4) we conclude that

$$\langle u^\infty - (v_1^\infty + v_2^\infty), \phi \rangle_{L^2(S^1)} = 0 \qquad \text{for all } \phi \in \mathcal{R}(P_1) \oplus \mathcal{R}(P_2) ,$$

i.e., $v_1^\infty + v_2^\infty$ is the best approximation of u^∞ in the closed subspace $\mathcal{R}(P_1) \oplus \mathcal{R}(P_2)$. Therefore,

$$\|u^\infty - (v_1^\infty + v_2^\infty)\|_{L^2(S^1)} \le \|u_1^\infty - P_1 u_1^\infty\|_{L^2(S^1)} + \|u_2^\infty - P_2 u_2^\infty\|_{L^2(S^1)}\,.$$

Applying Lemma 2.2, we find that

$$\|u_j^\infty - P_j u_j^\infty\|_{L^2(S^1)} \le \frac{r\sqrt{2}\pi}{\sqrt{N_j+1}} \left(\frac{e}{2\alpha}\right)^{N_j} \|f_j\|_{L^2(\mathbb{R}^2)}\,,$$

and, if $\alpha \ge e/2$ then the factor in front of the norm can be further estimated by q_j from above, completing the proof. $\qquad\qquad\qquad\qquad\qquad\qquad\qquad\qquad\square$

Since $\|P_1 P_2\| < 1$, (3.6) can be solved straightforwardly using fixed point iteration (with or without conjugate gradient acceleration), but we recommend solving the two equations directly. We describe this latter approach in more detail below and then discuss the conditioning of the problem in Section 4.

For $M, N \in \mathbb{N}$, let $T_{M,N}$ be the (rectangular) Toeplitz matrix

$$T_{M,N} = \begin{bmatrix} t_{M-N} & t_{M-N+1} & \cdots & t_{M+N} \\ t_{M-N-1} & t_{M-N} & & \\ \vdots & & \ddots & \\ \vdots & & & \\ t_{-M-N} & & \cdots & t_{-M+N} \end{bmatrix} \in \mathbb{R}^{(2M+1)\times(2N+1)} \qquad (3.8)$$

with entries

$$t_\nu = J_\nu(\kappa R)\,, \qquad \nu \in \mathbb{Z}\,,$$

We express $z = R(\cos\varphi_z, \sin\varphi_z)$ in polar coordinates and let $D_N \in \mathbb{C}^{(2N+1)\times(2N+1)}$ be the (unitary) diagonal matrix with diagonal entries

$$d_\nu = \mathrm{i}^\nu e^{\mathrm{i}\nu\varphi_z}\,, \qquad\qquad\qquad\qquad\qquad\qquad (3.9)$$

where ν runs from $-N$ to N. Then the matrix representation of $P_1 P_2 P_1$ restricted to the subspace $\mathcal{R}(P_1)$ can be decomposed as follows.

LEMMA 3.3. *Given $P_1 = Q_{N_1}$ and $P_2 = M_z^* Q_{N_2} M_z$ as above, let T_{N_2,N_1} be the Toeplitz matrix from (3.8) and D_{N_j}, $j = 1,2$, be the diagonal matrices introduced in (3.9). Then, the matrix representation of the operator $P_1 P_2 P_1$, restricted to $\mathcal{R}(P_1)$, with respect to the Fourier basis $\{e^{\mathrm{i}nt} : |n| \le N_j\}$ for $\mathcal{R}(P_1)$, is given by $D_{N_1}^* T_{N_2,N_1}^* T_{N_2,N_1} D_{N_1}$.*

Proof. Recalling (3.3) and (2.7) we represent a generic $\phi \in \mathcal{R}(P_1)$ by the vector $\mathbf{x} = [a_{-N_1}, \ldots, a_{N_1}]^T$ of its expansion coefficients with respect to the declared basis of $\mathcal{R}(P_1)$. Then $M_z P_1 \phi$ has the Fourier coefficients

$$\widetilde{a}_m = \sum_{n=-N_1}^{N_1} \mathrm{i}^{n-m} e^{\mathrm{i}(n-m)\varphi_z} J_{n-m}(\kappa R)\, a_n\,, \qquad m \in \mathbb{Z}\,,$$

cf. (2.13), and $Q_{N_2} M_z P_1 \phi$ cuts off all Fourier modes of $M_z P_1 \phi$ of order larger than N_2 in absolute value. Accordingly, $Q_{N_2} M_z P_1 \phi \in \mathcal{R}(Q_{N_2})$ is represented by the vector $\widetilde{\mathbf{x}} = D_{N_2}^* T_{N_2,N_1} D_{N_1} \mathbf{x}$ with entries $\widetilde{a}_m$, $-N_2 \le m \le N_2$, where T_{N_2,N_1}, D_{N_1} and D_{N_2} are defined as above.

It is easy to see that the operator M_z^* is the multiplication operator with the function $e^{-i\widehat{x}\cdot z}$ of (2.3), and hence, $P_2P_1\phi = M_z^*Q_{N_2}M_zP_1\phi$ equals

$$(P_2P_1\phi)(\widehat{x}) = \sum_{\nu=-\infty}^{\infty}(-\mathrm{i})^{\nu}e^{-\mathrm{i}\nu\varphi_z}J_{\nu}(\kappa R)e^{\mathrm{i}\nu t}\sum_{m=-N_2}^{N_2}\widetilde{a}_m e^{\mathrm{i}mt}$$

$$= \sum_{n=-\infty}^{\infty}\Big(\sum_{m=-N_2}^{N_2}\mathrm{i}^{m-n}e^{\mathrm{i}(m-n)\varphi_z}J_{n-m}(\kappa R)\,\widetilde{a}_m\Big)e^{\mathrm{i}nt}\,.$$

Therefore, $P_1P_2P_1\phi$ corresponds to the vector

$$\mathbf{y} = D_{N_1}^*T_{N_2,N_1}^*D_{N_2}\widetilde{\mathbf{x}} = D_{N_1}^*T_{N_2,N_1}^*T_{N_2,N_1}D_{N_1}\mathbf{x}\,,$$

and $P_1P_2P_1$ thus has the matrix representation $D_{N_1}^*T_{N_2,N_1}^*T_{N_2,N_1}D_{N_1}$. □

Using the decoupled formulation (3.6), the two individual far fields v_1^{∞} and v_2^{∞} approximating the components (3.1) of the given far field u^{∞} in the sense of (3.4) can be computed independently. In Algorithm 1 we suggest a numerical scheme to compute v_1^{∞}. The second component v_2^{∞} can be approximated analogously, after transforming the coordinate system and accordingly the far field pattern u^{∞} by means of the multiplication operator M_z from (2.12) such that a source radiating $M_z u_2^{\infty}$ is contained in $B_{r_2}(0)$.

Algorithm 1 Far field splitting for two sources

Suppose $u^{\infty} = u_1^{\infty} + u_2^{\infty}$ such that u_1^{∞} and u_2^{∞} are supported in $B_{r_1}(0)$ and $B_{r_2}(z)$, respectively.

1: **function** $v_1^{\infty} = $ SPLITTING2 $(u^{\infty}, \kappa, z, r_1, r_2)$
2:     Let $R = |z|$ and $N_0 = \lceil\alpha\kappa(R+r_2)\rceil$ for, say, $\alpha = e/2$.
3:     Compute the $2N_0+1$ lowest order Fourier coefficients of u^{∞}, and store the result in $\mathbf{a} = [a_{-N_0}, \ldots, a_{N_0}]^T$.
4:     Let D_{N_0}, D_{N_1} and T_{N_2,N_0}, T_{N_2,N_1} be diagonal and Toeplitz matrices as defined above, $\mathbf{b} = [a_{-N_1}, \ldots, a_{N_1}]^T$, and compute

$$\mathbf{c} = \mathbf{b} - D_{N_1}T_{N_2,N_1}^*T_{N_2,N_0}D_{N_0}\mathbf{a}\,.$$

5:     Solve the linear system

$$(I - D_{N_1}^*T_{N_2,N_1}^*T_{N_2,N_1}D_{N_1})\mathbf{x} = \mathbf{c}$$

    corresponding to (3.6a).
6:     The entries of $\mathbf{x}$ are the Fourier coefficients of the component v_1^{∞}.
7: **end function**

EXAMPLE 3.4. We illustrate Algorithm 1 by means of the following scattering problem. Suppose a kite-shaped and an ellipsoidal obstacle as shown in Fig. 3.2 (top left) are illuminated by an incoming plane wave from the left, the wave number being $\kappa = 5$, constant, in the exterior of the scatterers. Assuming that the kite is sound hard, while the ellipse is sound soft, the corresponding scattered field satisfies the homogeneous Helmholtz equation outside the obstacles, the Sommerfeld radiation condition at infinity, as well as a Neumann and a Dirichlet condition on the boundary
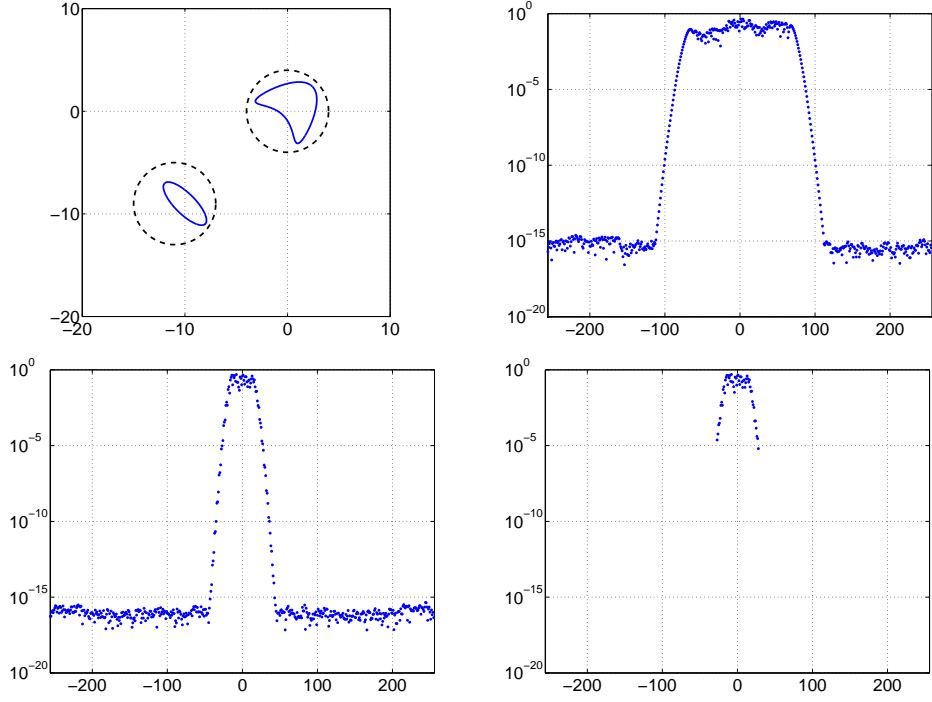
Fig. 3.2. *Top left: Geometry of the scatterers. Top right: Absolute values of the Fourier coefficients of u^∞. Bottom left: Absolute values of the Fourier coefficients of u_1^∞ (corresponding to the scatterer near the origin). Bottom right: Absolute values of the Fourier coefficients of v_1^∞.*

of the kite and the ellipse, respectively. We denote the scattered field by u^s and the corresponding far field pattern by u^∞.

It is well known that u^s can be written as a combined single and double layer potential with density on the boundary of the obstacles (see, e.g., [1]). This means that there exists a distributional source supported on the boundaries of the scatterers that radiates the far field pattern u^∞. On the other hand, multiplying u^s with a smooth cut-off function and substituting the result into the left hand side of (2.1a), it follows immediately that for any neighborhood of the obstacles there also exists a smooth source supported in this neighborhood that radiates u^∞ (see [12]). Accordingly u^∞ can be interpreted as a superposition of two far field patterns u_1^∞ and u_2^∞ radiated by two smooth sources supported in an arbitrarily small neighborhood of the two obstacles, respectively.

The absolute values of the Fourier coefficients of the far field pattern u^∞ are shown in Fig. 3.2 (top right). As has been mentioned before, and can nicely be seen in this plot, the Fourier coefficients decay superlinearly as soon as $|n| \geq 73 \approx \kappa\rho_0$, where ρ_0 denotes the radius of the smallest ball centered at the origin and containing both scatterers.

In Fig. 3.2 (bottom left) we include a plot of the absolute values of the Fourier coefficients of u_1^∞ radiated by the component of the source supported in an arbitrarily small neighborhood of the kite. To split the field numerically, we use the two dashed circles in the top left plot as a priori guesses for Algorithm 1, that is, we use the parameters $r_1 = r_2 = 4$ and $z = (-11, -9)$ in this algorithm. We choose $\alpha = e/2$ and

solve the linear system (3.6) directly. The absolute values of the Fourier coefficients of v_1^∞ are shown in Fig. 3.2 (bottom right). Note that the $e\kappa r_1 + 1 \approx 57$ lowest order Fourier coefficients of v_1^∞ agree very well with the corresponding Fourier coefficients of u_1^∞. ◇

4. The stability of the splitting problem. As mentioned before (see Lemma 3.1), problem (3.6a) has a unique (and well-posed) solution. However, since the far fields of all sources supported in *any* domain are dense in $L^2(S^1)$ (cf. Section 2), the norm of $P_1 P_2$ will get very close to one as we increase N_j in the definition of P_j, $j = 1, 2$. As we will see, however, the splitting problem is fairly well conditioned, as long as the two source components are well separated in a sense to be made precise below, cf. (4.1), and as long as the truncation indices N_j are well chosen, e.g.,

$$N_j = \lceil e\kappa r_j / 2 \rceil .$$

Our method can even tolerate more ill-conditioned regimes, as we will illustrate in Example 4.3 below.

The stability of the separation problem is measured in terms of the condition number of the linear systems (3.6) (cf. Algorithm 1) and the quality of the resulting approximations, cf. Lemma 3.2. As the condition number of the linear system depends on the spectral properties of (the finite rank operator) $P_1 P_2 P_1$ we now investigate the eigenvalues of its matrix representation $D_{N_1}^* T_{N_2,N_1}^* T_{N_2,N_1} D_{N_1}$, where T_{N_2,N_1} and D_{N_1} are as in (3.8)–(3.9). Note that these eigenvalues equal the squares of the singular values σ_j of T_{N_2,N_1}.

THEOREM 4.1. *Let $N_j = \lceil \alpha \kappa r_j \rceil$ for some fixed $\alpha > 0$, and assume that*

$$\delta := \max_{j=1,2} \frac{\kappa r_j^2}{R} \ll 1 . \tag{4.1}$$

Then the two dominating singular values $\sigma_{1/2}$ of T_{N_2,N_1} satisfy

$$\frac{2}{\pi} \frac{N_1 N_2}{\kappa R} - O(\delta^2) \leq \sigma_{1/2}^2 \leq \frac{2}{\pi} \frac{(N_1 + 1)(N_2 + 1)}{\kappa R} + O(\delta^2) ,$$

where the leading order term itself is $O(\delta)$.

Proof. In the range of indices $|m| \ll \sqrt{\kappa R}$ the Bessel functions $J_m(\kappa R)$ with fixed argument are oscillating with a wave length of about four,

$$t_m = J_m(\kappa R) = \left(\frac{2}{\pi \kappa R} \right)^{1/2} \cos(\kappa R - m\tfrac{\pi}{2} - \tfrac{\pi}{4}) \left(1 + O\left(\frac{m^2}{\kappa R} \right) \right) ,$$

cf., e.g., Gradshteyn and Ryzhik [3, 8.451]. In particular, as the index m of the entries t_m in T_{N_2,N_1} is bounded by $|m| \leq \lceil \alpha \kappa (r_1 + r_2) \rceil$, this happens to be the case when $\delta \ll 1$, and then, the entries of T_{N_2,N_1} satisfy

$$t_{N_2 - N_1 + 2m} = c \frac{(-1)^m}{\gamma} \left(1 + O(\delta) \right) ,$$

$$t_{N_2 - N_1 + 2m+1} = s \frac{(-1)^m}{\gamma} \left(1 + O(\delta) \right) ,$$

with uniform bounds on the error terms, where

$$\gamma = \sqrt{\tfrac{\pi}{2} \kappa R} ,$$

and

$$c = \cos\big(\kappa R - (N_2 - N_1)\tfrac{\pi}{2} - \tfrac{\pi}{4}\big), \qquad \text{and} \qquad s = \sin\big(\kappa R - (N_2 - N_1)\tfrac{\pi}{2} - \tfrac{\pi}{4}\big).$$

It follows that

$$\gamma T_{N_2,N_1} = C + E,$$

where C is the Toeplitz matrix

$$C = \begin{bmatrix} c & s & -c & -s & \cdots & (-1)^{N_1}c \\ -s & c & s & -c & & \vdots \\ -c & \ddots & \ddots & \ddots & & \vdots \\ \vdots & \ddots & & \ddots & \ddots & \vdots \\ \vdots & & & \ddots & \ddots & \vdots \\ (-1)^{N_2}c & & & & & (-1)^{N_1+N_2}c \end{bmatrix} \in \mathbb{R}^{(2N_2+1)\times(2N_1+1)},$$

and E is a matrix of the same size, with entries all of the order $O(\delta)$. Using the well known estimate

$$\|E\|^2 \leq \|E\|_\infty \|E\|_1,$$

where $\|E\|_\infty$ and $\|E\|_1$ denote the row- and column-sum norm, respectively, we conclude that

$$\gamma T_{N_2,N_1} = C + O(\sqrt{N_1 N_2}\,\delta),$$

respectively

$$T_{N_2,N_1} = \frac{1}{\gamma}C + O(\delta^{3/2}). \tag{4.2}$$

Obviously, the column rank of C is precisely two. We can determine an upper bound for the norm of C by embedding C in the Toeplitz matrix $\widetilde{C}$ that has one additional row and column and follows the same construction principle. $\widetilde{C}$ still has rank two, and it is easy to see that its (right) singular vectors are

$$\frac{\begin{bmatrix} 1 & 0 & -1 & 0 & 1 & 0 & \cdots \end{bmatrix}^T}{\sqrt{N_1+1}} \qquad \text{and} \qquad \frac{\begin{bmatrix} 0 & 1 & 0 & -1 & 0 & 1 & \cdots \end{bmatrix}^T}{\sqrt{N_1+1}},$$

while the associated (left) singular vectors are

$$\frac{\begin{bmatrix} c & -s & -c & s & c & -s & \cdots \end{bmatrix}^T}{\sqrt{N_2+1}} \qquad \text{and} \qquad \frac{\begin{bmatrix} s & c & -s & -c & s & c & \cdots \end{bmatrix}^T}{\sqrt{N_2+1}}.$$

The corresponding singular values are both equal to $\sqrt{(N_1+1)(N_2+1)}$, and hence we have determined the norm of $\widetilde{C}$. By the principle of Courant-Fischer this yields an upper bound for the norm of C. The same argument can be applied to the matrix that is obtained by deleting the last row and column of C. This then gives a lower bound for the norm of C, i.e.,
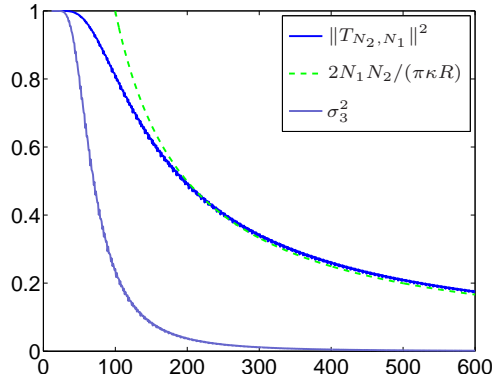
$$N_1 N_2 \leq \|C\|^2 \leq (N_1+1)(N_2+1).$$

FIG. 4.1. $\|T_{N_2,N_1}\|^2$ and σ_3^2 versus R; $r_1 = r_2 = 4$, $\kappa = 5$.

In fact, the two bounds apply to both (non-zero) singular values of C, and they turn out to be sharp in the sense that if $s = 0$ then the two bounds are precisely the two (distinct) singular values of C. Inserting this result into (4.2) the assertion follows. $\square$

REMARK 4.2. We conclude from Theorem 4.1 that the linear systems (3.6) are well conditioned, as long as

$$\frac{\kappa r_1 r_2}{R} = 2\pi \frac{(r_1/\lambda)(r_2/\lambda)}{R/\lambda}$$

is small, where $\lambda = 2\pi/\kappa$ is the associated wave length. Accordingly, this (necessarily unitless) quantity of interest relates the number of wavelengths in the diameters of the source supports, to the number of wavelengths that separate the two centers. Because the numerator is quadratic and the denominator is linear, increasing the wavelength, or equivalently, decreasing all sizes by the same scale, decreases the condition number.

$\diamond$

To further illustrate this result we include in Figure 4.1 a plot of the norm of T_{N_2,N_1} (strong solid line) and its estimate (strong dashed line) from Theorem 4.1 for $r_1 = r_2 = 4$, and $\kappa = 5$, where $N_j = \lceil e\kappa r_j/2 \rceil$, $j = 1, 2$ (that is, all parameters are as in Example 3.4), while the distance between the targets ranges from $R = 10$ up to $R = 600$. It can nicely be seen that the bound is pretty good until the estimate approaches one half.

We would like to recast this observation in a different form: The norm of $P_1 P_2$ is the cosine of the angle between the ranges of P_1 and P_2; if the norm is close to one, then the angle between the two subspaces is small, and there are far fields that belong to neither of the two subspaces but, at the same time, are very close to both of them. This is the case, for example, with far fields corresponding to sources that are supported half way between the centers of the two balls, i.e., at $x = z/2$, as soon as R approaches $r_1 + r_2$.

Finally, we mention that the third singular value σ_3 of T_{N_2,N_1} satisfies

$$\sigma_3^2 = O(\delta^3)$$

according to (4.2) and the proof of Theorem 4.1. A plot of σ_3^2 has also been included in Figure 4.1 as lighter solid curve. It is striking that $\sigma_3^2 \ll \sigma_2^2$ for a wide range of distances R.

EXAMPLE 4.3. We mention that in Example 3.4 above the two scatterers are not really well separated in the sense that the quantity δ of (4.1) be small. In fact, in this example we have $\delta = 5 \cdot 16/\sqrt{202} \approx 5.6 \gg 1$, and the condition number of $I - P_2 P_1 P_2$ is as large as 1.7×10^{12}! As the machine precision is about 10^{-16} this explains why the relative approximation error

$$\frac{\|u_1^\infty - v_1^\infty\|_{L^2(S^1)}}{\|u_1^\infty\|_{L^2(S^1)}} \approx 0.032 \tag{4.3}$$

for the approximation shown in Figure 3.1 is not too exciting; in fact this approximation error is about four orders of magnitude larger than the error of the best approximation $P_1 u_1^\infty$. Still, as we will see below in Section 6 this split is good enough to provide reasonable reconstructions of the two scatterers. $\diamond$

5. Multiple well-separated source terms. Suppose next that u^∞ from (2.2) is the superposition

$$u^\infty = u_1^\infty + \cdots + u_m^\infty$$

of m far fields $u_1^\infty, \ldots, u_m^\infty$ supported in well separated balls $B_{r_1}(z_1), \ldots, B_{r_m}(z_m)$, i.e., $|z_j - z_l| \gg r_j + r_l$ for $1 \leq j, l \leq m$, $j \neq l$.

Denoting by $P_j = M_{z_j}^* Q_{N_j} M_{z_j}$ the corresponding projections that generalize (3.3), we find as in Lemma 3.1 that $\|P_j P_l\| < 1$ for $1 \leq j \neq l \leq m$. The Galerkin formulation (3.4) can be generalized, seeking approximations $v_j^\infty \in \mathcal{R}(P_j)$ of u_j^∞, $j = 1, \ldots, m$, satisfying

$$\langle v_1^\infty + \cdots + v_m^\infty, \phi \rangle_{L^2(S^1)} = \langle u^\infty, \phi \rangle_{L^2(S^1)} \qquad \text{for all } \phi \in L^2(S^1),$$

which is equivalent to the system

$$\begin{aligned}
v_1^\infty + P_1 P_2 v_2^\infty + \cdots + P_1 P_m v_m^\infty &= P_1 u^\infty, \\
P_2 P_1 v_1^\infty + v_2^\infty + \cdots + P_2 P_m v_m^\infty &= P_2 u^\infty, \\
&\vdots \\
P_m P_1 v_1^\infty + P_m P_2 v_2^\infty + \cdots + v_m^\infty &= P_m u^\infty.
\end{aligned} \tag{5.1}$$

Again, a Neumann series argument reveals that (5.1) is uniquely solvable if $\|P_j P_l\| < 1/(m-1)$ for all $1 \leq j \neq l \leq m$. The system can be solved iteratively using, e.g., the Gauss-Seidel method, or a direct solver, once the block matrix corresponding to the entire linear system has been assembled. The latter can be achieved by following the argument of the proof of Lemma 3.3.

6. A numerical procedure to approximate well-separated scatterers. Having shown how to split a given far field into its individual components radiated from well-separated source terms, we now suggest a numerical scheme to approximate the individual sources themselves, and use the particular Example 3.4 for demonstration. In all our computations the exact far field pattern u^∞ has been computed on an equidistand grid with 512 points on the unit circle using the Nyström method as described in [1, 7]. (The number of grid points must be sufficiently large to resolve all relevant Fourier modes, cf. Figure 3.2.) This implementation of the forward problem also provides easy access to equivalent sources that generate the individual far field components u_j^∞, $j = 1, 2$, one of which is displayed in terms of its Fourier coefficients in Figure 3.2.

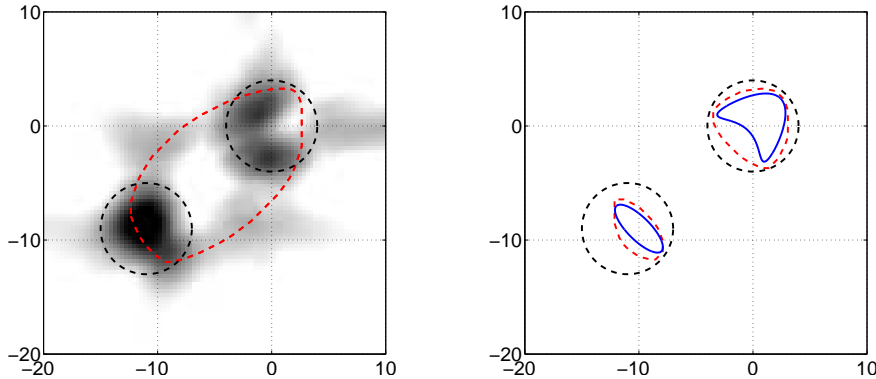Our method consists of three steps that we now describe in more detail.

FIG. 6.1. *Left: Inverse Radon approximation (gray scale), convex scattering support of u^∞ (dashed line), and a priori guess of source positions (dashed circles). Right: A priori guess of source positions (dashed circles), convex scattering supports of u_1^∞, u_2^∞ (dashed lines), and geometry of the scatterers (solid lines).*

6.1. Step 1: The a priori guess. To begin with we utilize a rather crude inversion scheme, namely the inverse Radon approximation suggested in [4], to provide a means to estimate the number of individual source components, together with their approximate location and size. Concerning Example 3.4 this "reconstruction" is shown as gray scale image in Figure 6.1 (left). The inverse Radon algorithm has been implemented as described in [4], using the window size $\varepsilon = \pi/15$ (for the involved windowed Fourier transform of the far field, given $\kappa = 5$).

The lighter dashed line included in this plot is the boundary of the convex scattering support $\mathscr{C}(u^\infty)$. Our implementation of the convex scattering support essentially follows [9]: First a rough estimate for the domain of interest, where the scatterers are expected to be, is obtained from the modulus of the Fourier coefficients of u^∞ shown in Fig. 3.2 (top right). Observing that the superlinear decay starts around $|n| = 73$, we expect that the convex scattering support $\mathscr{C}(u^\infty)$ is contained in a circle with a radius of about $\rho_0 = 73/\kappa = 14.6$ around the origin. We now pick 32 evenly spaced points $\zeta_1, \ldots, \zeta_{32}$ on that circle. For each of them we transform the coordinate system by shifting this point ζ_ℓ into the origin, and transform the far field pattern u^∞ with the multiplication operator M_{ζ_ℓ} from (2.12) accordingly. Then we count the Fourier coefficients $\widetilde{a}_n$ of the transformed far field that are effectively non-zero. To this end we define

$$m_{\zeta_\ell} := \min\Big\{m \in \{0, \ldots, 255\} \;\Big|\; \sum_{n=-m}^{m} |\widetilde{a}_n|^2 \Big/ \sum_{n=-255}^{256} |\widetilde{a}_n|^2 \geq 1 - \eta \Big\}, \qquad (6.1)$$

where $\eta = 10^{-4}$ is a threshold parameter that has to be chosen appropriately (depending, in particular, on the noise level in the data). Finally we let $\rho_\ell = m_{\zeta_\ell}/\kappa$, and approximate the convex scattering support of u^∞ by

$$\mathscr{C}(u^\infty) \approx \bigcap_{\ell=1}^{32} B_{\rho_\ell}(\zeta_\ell). \qquad (6.2)$$

Based on the results of the inverse Radon reconstruction in Figure 6.1 we start with the assumption that there are two separate source components located in a

neighborhood of the two points $z = (-11, -9)$ and the origin, respectively. The shape of the convex scattering support gives additional information on their dimension. We use this information to choose sufficiently large circles around the aforementioned two points, namely we pick the radii $r_1 = r_2 = 4$ which yields the initial guess shown in Figure 3.2 (upper left) and in Figure 6.1 (left; dashed circles).

6.2. Step 2: Splitting the far field. The split of the far field $u^\infty \approx v_1^\infty + v_2^\infty$ is performed as described in Algorithm 1; the two circles determined in Subsection 6.1 provide the parameters that have been used in Example 3.4, and the far fields v_j^∞ correspond to sources as in (2.8) supported in the two respective disks. See Example 3.4 for further details.

6.3. Step 3: Approximating the individual sources/scatterers. Once the far field has been split into its individual components, one can apply her or his favorite method of choice to reconstruct associated source components. Here we choose to estimate the individual scatterers by computing the convex scattering supports $\mathscr{C}(u_1^\infty)$ and $\mathscr{C}(u_2^\infty)$, using the far field patterns v_1^∞ and v_2^∞ resulting from Step 2 (Subsection 6.2) separately. For this we utilize the same implementation as in Subsection 6.1, except that we choose the points ζ_ℓ of (6.2) from the circles $\partial B_{r_j}(z_j)$, $j = 1, 2$, that have been determined in Step 1. (In Example 3.4, $z_1 = 0$, and $z_2 = (-11, -9)$; $r_1 = r_2 = 4$.)

The outcome for Example 3.4 is shown in Fig. 6.1 (right) (non-circular dashed lines) together with the true scatterer geometries (solid lines) to allow for a better appreciation of this result. The convex scattering supports of u_1^∞ and u_2^∞ provide a surprisingly good impression of location and shape of the true scatterers.

In view of the discussion in Example 4.3 it has to be emphasized that the two scatterers of this particular phantom are not well-separated in the sense introduced in Theorem 4.1. In fact, due to the huge condition number of the linear systems (3.6), the approximations v_j^∞ of u_j^∞ are not very accurate, cf. (4.3). This loss of accuracy, however, does not seem to spoil the overall performance of the method.

A final comment is in order: As mentioned before, the computed far field patterns v_1^∞ and v_2^∞ correspond to sources as in (2.8), and their exact convex source support degenerates to the two points $\mathscr{C}(v_1^\infty) = \{0\}$ and $\mathscr{C}(v_2^\infty) = \{z\}$. Our approximation (6.2) does, in fact, provide a different result that is much more useful. The reason for this is that, in the criterion (6.1), the threshhold parameter η limits the L^2 norm of the source that radiates the far field . This is a physically appropriate condition that depends on all the coefficients, whereas the range condition only requiress that the coefficients decay sufficiently fast asymptotically, which only depends on the highest coefficients, the ones that are most sensitive to noise.

7. More numerical results. As another example we consider a scattering problem with three obstacles (an ellipsoid, a kite, and a nut) as shown in Fig. 7.1 (left) that are illuminated by one incoming plane wave from the left. The kite and the nut are assumed to be sound hard, while the ellipsoid is sound soft. As outlined in Example 3.4 the corresponding far field pattern u^∞ can be written as a superposition of three far field patterns u_j^∞, $j = 1, 2, 3$, radiated by three individual smooth sources supported in arbitrarily small neighborhoods of the three scatterers.

We emphasize that size and orientation of the kite and the ellipse are exactly the same as in the other example. However, the distance between the obstacles has been increased as compared to Example 3.4 in order to reduce the ill-conditioning of the splitting problem.
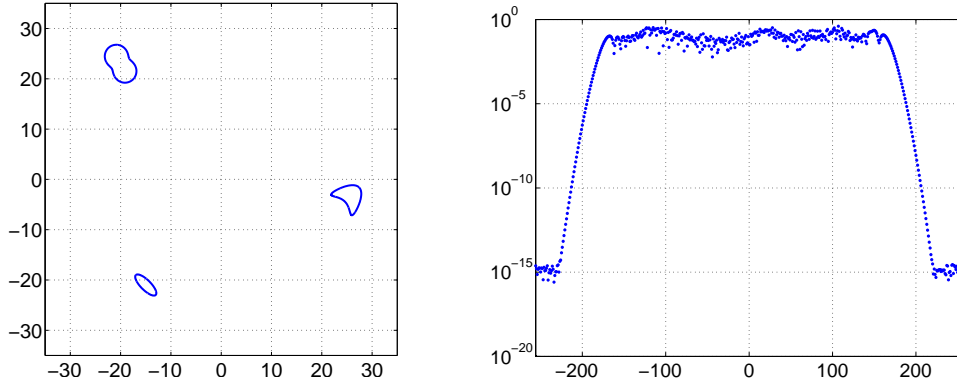
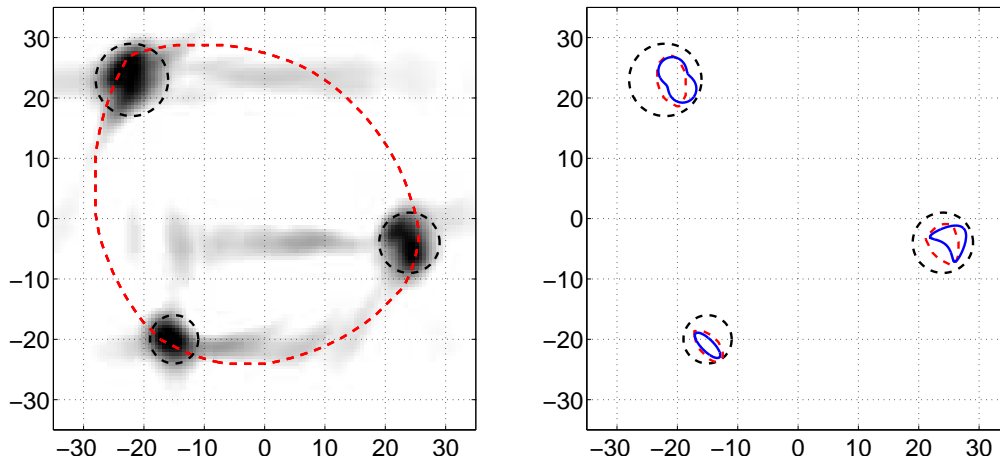FIG. 7.1. *Left: Geometry of the scatterers. Right: Absolute values of the Fourier coefficients of u^∞.*

FIG. 7.2. *Left: Inverse Radon approximation (gray scale), convex scattering support of u^∞ (dashed line), and a priori guess of source positions (dashed circles). Right: A priori guess of source positions (dashed circles), convex scattering supports of u_1^∞, u_2^∞, and u_3^∞ (dashed lines), and geometry of the scatterers (solid lines).*

The simulation of the forward problem is done in the same way as in the other example, and the Fourier coefficients of u^∞ are shown in Fig. 7.1 (right).

In this example we had to slightly modify the numerical computation of the convex scattering support $\mathscr{C}(u^\infty)$ of the overall far field in Step 1 of our inversion procedure, in that we picked the points ζ_ℓ of (6.2) from a circle around the origin with radius $\rho_0/2$, where ρ_0 is the smallest concentric circle enclosing all three scatterers. The reason for this is that otherwise we would have had to further subsample the far field to get enough frequency information, a price we haven't been willing to pay. This modification does affect the result in that the approximation of the convex scattering support is somewhat too "roundish". See Fig. 7.2 (left). Still it is sufficient for determining reasonable a priori inclusions of the true scatterers. We estimate approximate locations of three individual sources as indicated by the dashed circles with radii $r_1 = 4$, $r_2 = 5$, and $r_3 = 6$ in Fig. 7.2 (left).

Next we compute approximations v_j^∞ of u_j^∞, $j = 1, 2, 3$, by solving the linear block
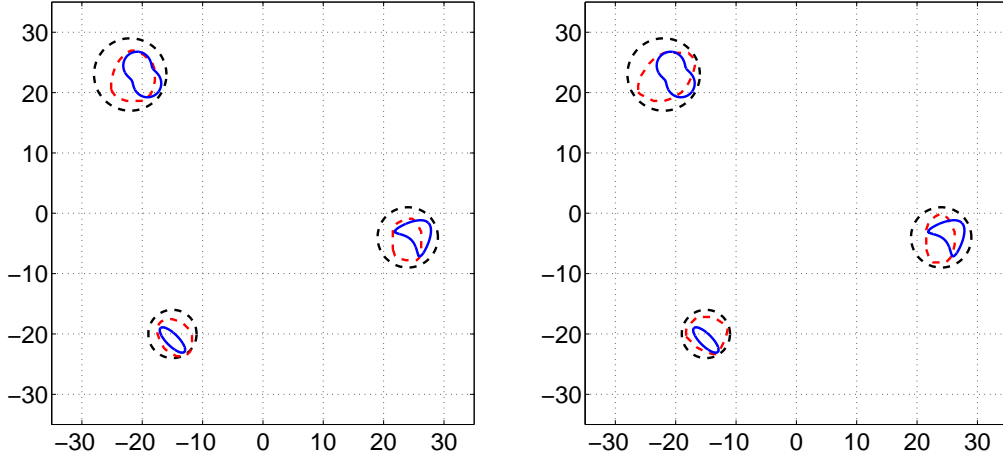
FIG. 7.3. *Left: Same as Fig. 7.2 (right), but using data containing* 1% *uniformly distributed noise. Right: Same as Fig. 7.2 (right), but using data containing* 5% *uniformly distributed noise.*

system (5.1). The condition number of the corresponding matrix is still quite large, but its value 3.2×10^4 is considerably smaller than in the other example. Accordingly, the resulting approximation is much better than in the previous example:

$$\frac{\|u_\infty - (v_1^\infty + v_2^\infty + v_3^\infty)\|_{L^2(S^1)}}{\|u^\infty\|_{L^2(S^1)}} \approx 1.1 \times 10^{-6} \,.$$

The convex scattering supports $\mathscr{C}(u_j^\infty)$, $j = 1, 2, 3$, computed from the split far fields v_j^∞, $j = 1, 2, 3$ – using the same threshold parameter $\eta = 10^{-4}$ in (6.1) as before – are shown in Fig. 7.2 (right) (dashed lines) together with the true scatterers (solid lines). These convex scattering supports are decent reconstructions of the true scatterers.

To get an idea about the sensitivity of the algorithm with respect to noise in the data, we redo this computation but add uniformly distributed relative error to the simulated forward data before splitting the far field pattern. We use the same a priori guess for the scatterers as before. The resulting convex scattering supports $\mathscr{C}(u_j^\infty)$, computed from the corresponding approximations v_j^∞, $j = 1, 2, 3$, are shown in Fig. 7.3 for two different noise levels. In these reconstructions the noise is only accounted for via the threshold parameter η of (6.1): while we can still use $\eta = 10^{-4}$ for 1% noise, we choose $\eta = 10^{-3}$ for 5% noise.

The results clearly get worse with increasing noise level, but they still contain useful information on the scatterers.

8. Conclusions. We have treated the source problem for the Helmholtz equation in the plane when the source is the union of finitely many well-separated components with compact support. We have presented a fairly simple algorithm to approximately split the far field pattern radiated by this source into the far fields corresponding to the individual source components. The conditioning of this problem depends on the dimensions of the source components and their relative distances. Notably, the condition is not invariant under scaling. Increasing sizes, or equivalently, decreasing wavelength, increases the condition number.

We also suggested an overall procedure to, (i), estimate the number of distinct

source components, as well as their size and location, (ii), split the given far field accordingly, and (iii), approximate the individual convex source supports of the respective source components as the final output.

Numerical tests for inverse obstacle scattering, using phantoms consisting of more than one scatterer, have demonstrated the potential of this method. We emphasize that the reconstructions are computed from a single far field pattern, corresponding to a single excitation, and that the method does not require any a priori information on physical or topological properties of the scatterers.

Appendix. Here we prove an inequality for the superlinear decay of the Bessel functions for fixed argument and large index that we haven't been able to find in the literature.

THEOREM A.1. *For any $n \in \mathbb{Z} \setminus \{0\}$ and every fixed positive real number r there holds*

$$|J_n(r)| \leq \left(\frac{er}{2|n|}\right)^{|n|}, \qquad n \in \mathbb{Z} \setminus \{0\},$$

Proof. By definition there holds

$$J_n(r) = \frac{1}{2\pi} \int_0^{2\pi} e^{i(r\sin\theta - n\theta)} \, d\theta,$$

and without loss of generality we can assume that n is positive, because $J_{-n}(r) = (-1)^n J_n(r)$. The argument of the above integral being an analytic function of θ, we can integrate along the boundary of the rectangle with vertices at $\theta = 0$, $\theta = \pi$, and $\theta = it$ with $t < 0$ to obtain

$$J_n(r) = \frac{1}{2\pi} \int_0^{2\pi} e^{i\left(r\sin(\theta + it) - n(\theta + it)\right)} \, d\theta$$

$$+ \frac{1}{2\pi} \int_0^t e^{i\left(r\sin(i\tau) - ni\tau\right)} \, d\tau - \frac{1}{2\pi} \int_0^t e^{i\left(r\sin(2\pi + i\tau) - 2\pi n - ni\tau\right)} \, d\tau$$

$$= \frac{1}{2\pi} e^{nt} \int_0^{2\pi} e^{ir\sin(\theta + it)} e^{-in\theta} \, d\theta$$

$$= \frac{1}{2\pi} e^{nt} \int_0^{2\pi} e^{ir\sin\theta\cosh t} e^{-r\cos\theta\sinh t} e^{-in\theta} \, d\theta.$$

Turning to absolute values we find

$$|J_n(r)| \leq \frac{1}{2\pi} \int_0^{2\pi} e^{nt - r\cos\theta\sinh t} \, d\theta \leq e^{nt + r|\sinh t|} \leq \exp\left(nt + \frac{1}{2}re^{-t}\right);$$

remember that t has been chosen to be negative. For $n > r/2$ this upper bound attains its minimal value when $e^{-t} = 2n/r$, hence

$$|J_n(r)| \leq \left(e^{-t}\right)^{-n} e^n = \left(\frac{er}{2n}\right)^n,$$

as has been claimed. For $0 < n < r/2$, on the other hand, this inequality holds trivially, as

$$|J_n(r)| \leq \frac{1}{2\pi} \int_0^{2\pi} d\theta = 1 \leq e^n \leq \left(\frac{er}{2n}\right)^n,$$

as $r/(2n)$ is greater than one in this case. Of course, this means that the inequality provides independent information only for $n > er/2 \approx 1.3591\,r$.   □

REFERENCES

[1] D. COLTON AND R. KRESS, *Inverse Acoustic and Electromagnetic Scattering Theory*, 2nd ed., Springer, Berlin, 1998.

[2] F. DEUTSCH, Rate of convergence of the method of alternating projections, in B. Brosowski and F. Deutsch (eds.), *Parametric Optimization and Approximation. Proceedings, Oberwolfach, 1983.*, Birkhäuser-Verlag, Basel, 1985, pp. 96–107.

[3] I.S. GRADSHTEYN AND I.M. RYZHIK, *Table of Integrals, Series, and Products*, 7th ed., Academic Press, New York, 2007.

[4] R. GRIESMAIER, T. RAASCH, AND M. HANKE, Inverse source problems for the Helmholtz equation and the windowed Fourier transform, *SIAM J. Sci. Comput.*, 34 (2012), A1544–A1562.

[5] M. HANKE, One shot inverse scattering via rational approximation, *SIAM J. Imaging Sci.*, 5 (2012), 465–482.

[6] F. BEN HASSEN, J. LIU, AND R. POTTHAST, On source analysis by wave splitting with applications in inverse scattering of multiple obstacles, *J. Comput. Math.*, 25 (2007), 266-281.

[7] R. KRESS, On the numerical solution of a hypersingular integral equation in scattering theory, *J. Comput. Appl. Math.*, 61 (1995), 345–360.

[8] S. KUSIAK AND J. SYLVESTER, The scattering support, *Comm. Pure Appl. Math.*, 56 (2003), 1525–1548.

[9] S. KUSIAK AND J. SYLVESTER, The convex scattering support in a background medium, *SIAM J. Math Anal.*, 36 (2005), 1142–1158.

[10] R. POTTHAST, F. M. FAZI, AND P. A. NELSON Source splitting via the point source method, *Inverse Problems*, 26 (2010), 045002.

[11] R. POTTHAST, J. SYLVESTER, AND S. KUSIAK, A "range test" for determining scatterers with unknown physical properties, *Inverse Problems*, 19 (2003), 533-547.

[12] J. SYLVESTER, Notions of support for far fields, *Inverse Problems*, 22 (2006), 1273–1288.